

Tortuosity of unsaturated porous fractal materials

S. W. Coleman* and J. C. Vassilicos

Department of Aeronautics and Institute for Mathematical Sciences, Imperial College, London, SW7 2BY, United Kingdom

(Received 6 November 2007; published 18 July 2008)

The tortuosity of a capillary-condensed film of inviscid fluid adsorbed onto fractal substrates as a function of the filling fraction of the fluid has been calculated numerically. This acts as a way of probing the multiscale structure of the objects. It is found that the variation of tortuosity α with filling fraction ϕ is found to follow a power law of the form $\alpha \sim \phi^{-\epsilon}$ for both deterministic and stochastic fractals. These numerically calculated exponents are compared to exponents obtained from a phenomenological scaling and good agreement is found, particularly for the stochastic fractals.

DOI: [10.1103/PhysRevE.78.016308](https://doi.org/10.1103/PhysRevE.78.016308)

PACS number(s): 47.90.+a, 61.43.Gt, 61.43.Hv, 66.30.-h

I. INTRODUCTION

There has been considerable interest recently in the unusual transport properties of porous fractal materials. Understanding the correlation between these properties and the material's microstructure is crucial for their use to become widespread. Examples of man-made porous fractal materials include aerogel [1] and metal foams [2], while naturally occurring examples include fracture surfaces [3] and the lungs [4]. In all these cases the multiscale structure has a significant impact on important properties. For example, the permeability of a fracture, which is used to determine macroscopic flow rates through porous materials, is substantially increased if the fracture interface has fractal characteristics [5]. Moreover, multiscale materials can possess remarkable transport properties (thermal conductivity and permeability for example) when compared to more conventional materials. Aerogel, for instance, is 39 times more insulating than the best fiberglass, yet 1000 times less dense [6]. The characterization of porous materials and their transport properties has historically been limited to the measurement of macroscopic parameters, which tells one little about the mesoscopic structure of these materials. There has been much progress [7,8] in using microtomography images to generate three-dimensional (3D) networks from which flow properties can be predicted. However, it is not always easy to draw a relationship between observable transport properties and simple geometrical quantities. Furthermore, despite the advances mentioned, predictions of these properties are still largely based on empirical relationships based on observable characteristics of the geometry, such as porosity [9].

Aerogel is of particular interest in this work. An experimental technique has recently been described [10], which measures the tortuosity, defined momentarily, of various samples of aerogel as a function of the volume filling fraction ϕ of an adsorbed superfluid ^4He film on the surface of the aerogel. Tortuosity α quantifies the tortuous or twisted nature that a fluid has to take to pass through a porous material. There are many ways this twisted path can be quantified, with perhaps the most obvious being the length of the actual paths of fluid molecules. In both [10] and this work

tortuosity is defined as a dimensionless quantity which quantifies the added mass effect caused by fluid flowing around an obstruction [11], $\alpha = \frac{\rho^*}{\rho_f}$, where ρ^* is the effective density caused by the added mass effect and ρ_f is the bulk fluid density. The added mass effect simply describes the inertial (as opposed to viscous) drag that the porous material exerts on the fluid as the latter is accelerated relative to the former [12]. Suitably normalized, this added mass is a quantity *which only depends on the geometry of the porous material*. For a straight, nonobstructed flow path $\alpha = 1$, whereas for any twisted flow path $\alpha > 1$. As will be seen later, tortuosity has a simple physical interpretation of the ratio of the kinetic energies of an unobstructed flow to the actual tortuous flow through the porous medium.

The idea of calculating the tortuosity of a fractal porous material with varying amounts of adsorbed fluid is as follows: when the fractal is saturated with fluid, the majority of the fluid only “sees” the large scale features of the flow. If thinner helium films are deposited on the fractal surface, then gradually small scale features of the fractal become important. In this way, the film thickness acts as a way of probing different length scales of the fractal. This “defractalization” idea is shown schematically in Fig. 1. It was found in [10] that the tortuosity scaled with the volume of condensed helium as a power law, with an exponent close to -1 . This can be treated as the scaling of a dynamical property, i.e., a transport property, in a fractal environment.

A phenomenological argument has been given by the authors [13] for how the tortuosity varies with the filling fraction ϕ of fluid in the porous medium, with the exponent being a function of the box-counting dimension D_f (see [14]

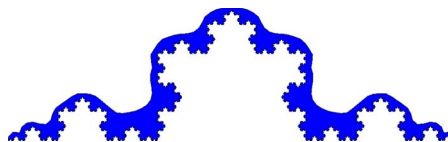


FIG. 1. (Color online) Schematic representation of the adsorption of a liquid film on a fractal surface, with the shaded area representing the adsorbed fluid. As the film thickness increases smaller scale features become less important. The Koch curve has been used for ease of representation, although this is a surface fractal, as opposed to the mass fractal structure being considered in this work.

*stuart.coleman@imperial.ac.uk

for definition) and the random walk dimension D_w . D_w is defined by considering the diffusion constant D of a random walker, whose average mean square displacement $\langle R^2(t) \rangle = Dt$. When this random walker is constrained to a fractal network, D becomes dependent on the distance L traveled by the random walker, $D(L) \sim L^{2-D_w}$, where $D_w=2$ for a non-fractal object [15]. There are three key statements needed to obtain the scaling: (i) $D(L) \sim L^{2-D_w}$ is range dependent on a fractal object, (ii) $D(L)$ is related to electrical conductivity $\sigma(L)$ via the Einstein relation, $D(L) = [k_B T \sigma(L)] / [qn(L)]$, where k_B is Boltzmann's constant, T is the temperature, $n(L)$ is the concentration of current carrying particles, and q their charge, and (iii) that the equivalence between the hydrodynamical problem of an inviscid, incompressible fluid flowing in a pore space and that of the electrical conductivity σ of a nonconducting, rigid porous material, containing a conducting pore fluid of conductivity σ_f allows the tortuosity α to be expressed as $\alpha = \frac{\sigma_f}{\sigma} \phi$ [16,17]. The explicit form of the scaling obtained is

$$\alpha \sim \phi^{(D_w-2)/(D_f-d_E)}, \quad (1)$$

where d_E is the Euclidean dimension.

This paper aims to investigate the validity of this relationship between the scaling of tortuosity and the fractal characteristics of the adsorbant material. This is done by using both the phenomenological scaling argument given in Eq. (1) and numerical simulations. The structure of the paper is as follows: the numerical techniques are briefly discussed in the next section, followed by a brief discussion on the significance of tortuosity. We then present our results on the range of validity of Eq. (1).

II. NUMERICAL TECHNIQUES

A. Lattice gas model

In order to simulate the experiments of [10] numerically, it is necessary to have a model of the fractal-adsorbant system. The morphology of an adsorbed liquid film is governed by the capillary forces, van der Waals forces, and chemical potential of the liquid, where gravity is neglected, as it has been shown to have no effect on the adsorption process in aerogel [18]. It is particularly important that the geometrical complexity of the problem is retained as this is crucial to determining the tortuosity of a given fractal. This eliminates the possibility of using network models, where the porous material is modeled as a collection of independent pores of simple geometry but varying sizes, given by the pore size distribution, as in [19].

The method we use is virtually identical to that developed in [20], which incorporates the essential physical ingredients, in particular the energetic and geometric disorder of the solid. We consider the Hamiltonian of a simple lattice-gas model in the presence of geometrical disorder. Only the energies due to fluid-fluid interaction and solid-fluid interaction, of strengths w_{ff} and w_{sf} , respectively, between nearest neighbors on the lattice, are considered. The Hamiltonian is

$$H = -w_{ff} \sum_{i<j}^{nn} \tau_i \tau_j \eta_i \eta_j - w_{sf} \sum_{i<j}^{nn} [\tau_i \eta_j (1 - \eta_j) + \tau_j \eta_i (1 - \eta_i)], \quad (2)$$

where the sums run over nearest-neighbor sites. τ_i is a fluid occupation variable, which indicates whether site i of the lattice is occupied by fluid ($\tau_i=1$) or not ($\tau_i=0$). η_i is a quenched variable that characterizes the presence of solid particles at site i ($\eta_i=0$ if solid is present and $\eta_i=1$ if not).

The thermodynamic behavior of the fluid in the presence of the geometric disorder is given by the solution of Eq. (2) in the grand canonical ensemble, which is treated using local mean field theory (LMFT) [21], leading to a set of N coupled nonlinear equations for the densities $\rho_i = \langle \tau_i \eta_i \rangle$, where $\langle \dots \rangle$ denotes ensemble average.

$$\rho_i = \frac{1}{1 + e^{-X_i}}. \quad (3)$$

Here $X_i = \beta \{ \sum_j^{nn} [w_{ff} \rho_j + w_{sf} (1 - \eta_j)] + \mu \}$. For a given configuration of porous material, described by the set η_i , the sorption isotherms

$$\rho_f(\mu, T) = \frac{1}{N} \sum_i \rho_i \quad (4)$$

are obtained by increasing or decreasing the chemical potential in steps $\delta\mu$ and using an iteration procedure to solve the equations. The initial condition is all nongel sites empty for adsorption ($\rho_i=0$) and all nongel sites full for desorption ($\rho_i=1$). At each subsequent μ , the converged solution at $\mu - \delta\mu$ for adsorption or $\mu + \delta\mu$ for desorption is used to start the iterations.

It has been shown in [22,23] that the usual periodic boundary conditions, employed in [24], for example, are not acceptable for the simulation of desorption isotherms, as they suppress nucleation of the low density phase and therefore display greatly exaggerated hysteresis. In order to prevent this, one surface of the simulated system is connected to a reservoir of bulk vapor for desorption calculations [23]. This condition is implemented in the z direction, while in the x and y directions periodic boundary conditions are used. For ease of implementation of the finite element method described in the next section, a square lattice has been used for the 2D case, and a simple cubic for the 3D case.

B. Obtaining the velocity field

Having obtained the morphology of the adsorbed fluid film, the calculation of the velocity field of the fluid consists of the solution of the equations of fluid motion, with the geometry defined by the presence of fluid sites on the lattice-gas model of adsorption described in the previous section. We introduce the velocity potential ψ , defined so that $\nabla\psi = \mathbf{v}$, where \mathbf{v} is the velocity field of an incompressible, inviscid fluid through the porous medium due to an applied pressure gradient. The porous medium occupies the space $0 < x < L$, where L is large compared to the size of the pores, and has a total lateral area A . A potential difference ψ_L is applied across the porous medium and zero-flux boundary conditions

are enforced on all other boundaries. The conditions of incompressibility and irrotationality associated with the superfluid ⁴He lead to a classic potential problem for the velocity potential ψ , which has been solved using standard finite element schemes [25]

The filling fraction ϕ is defined by considering the function $\gamma(\mathbf{r})$, which is equal to 1 when \mathbf{r} is occupied by fluid and 0 elsewhere. Clearly, $\phi = \frac{1}{LA} \int \gamma(\mathbf{r}) d^3\mathbf{r}$. The function $\gamma(\mathbf{r})$ can be seen to be closely related to the fluid occupancy variable ρ_i of the previous section. In fact, ρ_i is simply a discretized version of $\gamma(\mathbf{r})$ on the lattice.

III. TORTUOSITY

As stated previously, the tortuosity used in this work is a measure of the added mass effect caused when a fluid is accelerated around a solid object. This added mass effect is caused by the inertial drag that the solid exerts on the fluid [12]. In the case where the solid object is rigid, i.e., its displacement can be neglected, it has been shown [26] that the effective density ρ^* of the fluid due to the added mass effect is given by $\rho^* = \alpha \rho_f$, where ρ_f is the bulk fluid density and $\alpha \geq 1$ is a purely geometrical quantity independent of fluid or solid densities. This is the tortuosity considered in this work.

An expression for the tortuosity based on the velocity field is more convenient for our purposes. The tortuosity defined above can be considered as the ratio of the kinetic energy of an equivalent unobstructed flow to the kinetic energy of a flow that has to follow the tortuous path and thus has a higher effective density. Using this, a relationship has been obtained for the tortuosity of a fluid in a fully saturated pore space in [11]. Here, these arguments are extended to

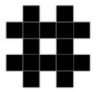
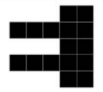
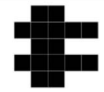
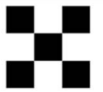

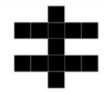
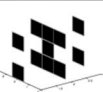
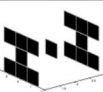
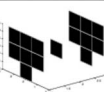
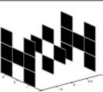
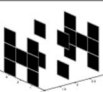
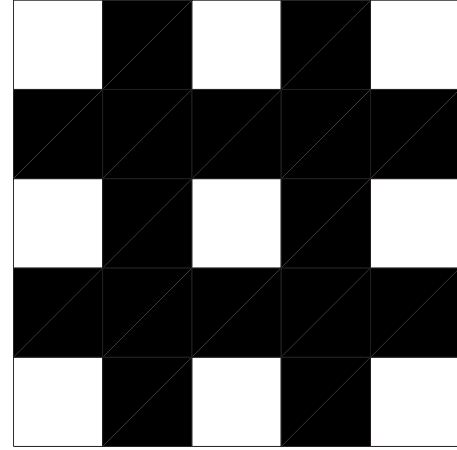
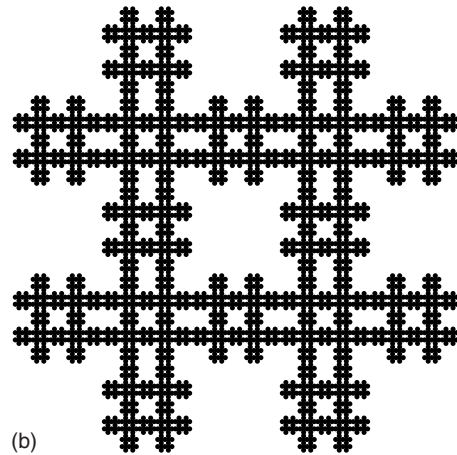
			
ϵ_{pre}	1.64	1.40	1.39
ϵ_{num}	1.69	1.30	1.25
			
ϵ_{pre}	1.10	1.20	1.15
ϵ_{num}	0.98	0.92	1.27
			
ϵ_{pre}	0.67	0.43	0.87
ϵ_{num}	0.54	0.42	0.92
			
ϵ_{pre}	1.21	0.71	
ϵ_{num}	0.50	0.72	

FIG. 2. The generators of the fractals used for unsaturated simulations, along with the numerically obtained tortuosity-filling fraction ϵ_{num} and the predicted exponent ϵ_{pre} .



(a)



(b)

FIG. 3. Illustration of the generation of deterministic fractals from the generator for the unsaturated simulations. (a) $n=1$, (b) $n=4$.

take account of a partially saturated pore space.

Solving the potential problem for the tortuous flow, the kinetic energy of the tortuous flow is given by $E(\psi) = \frac{1}{2} \rho_f \int \gamma(\mathbf{r}) (\nabla \psi)^2 d^3\mathbf{r}$. A porous material whose pores were all straight and perfectly aligned with the direction of the incoming flow would provide zero resistance to the flow. The velocity would only be nonzero in the x direction and would be given by $\frac{\partial \psi}{\partial x} = \frac{\psi_L}{L}$. Taking the ratio of the kinetic energies of the two flows gives

$$\alpha = \frac{\phi A (\psi_L)^2}{L \int \gamma(\mathbf{r}) (\nabla \psi)^2 d^3\mathbf{r}} \quad (5)$$

This reduces to the expression given in [11] when the pores are saturated with fluid, i.e. $\phi = \mathcal{P}$, where \mathcal{P} is the porosity of the material. It should be noted that definitions of tortuosity using the resistivity or acoustic properties of the fluid saturated porous material are equivalent to this hydrodynamic definition [16,26].

IV. RESULTS

Results are now presented from the numerical simulations of adsorption in stochastic and deterministic fractal environ-

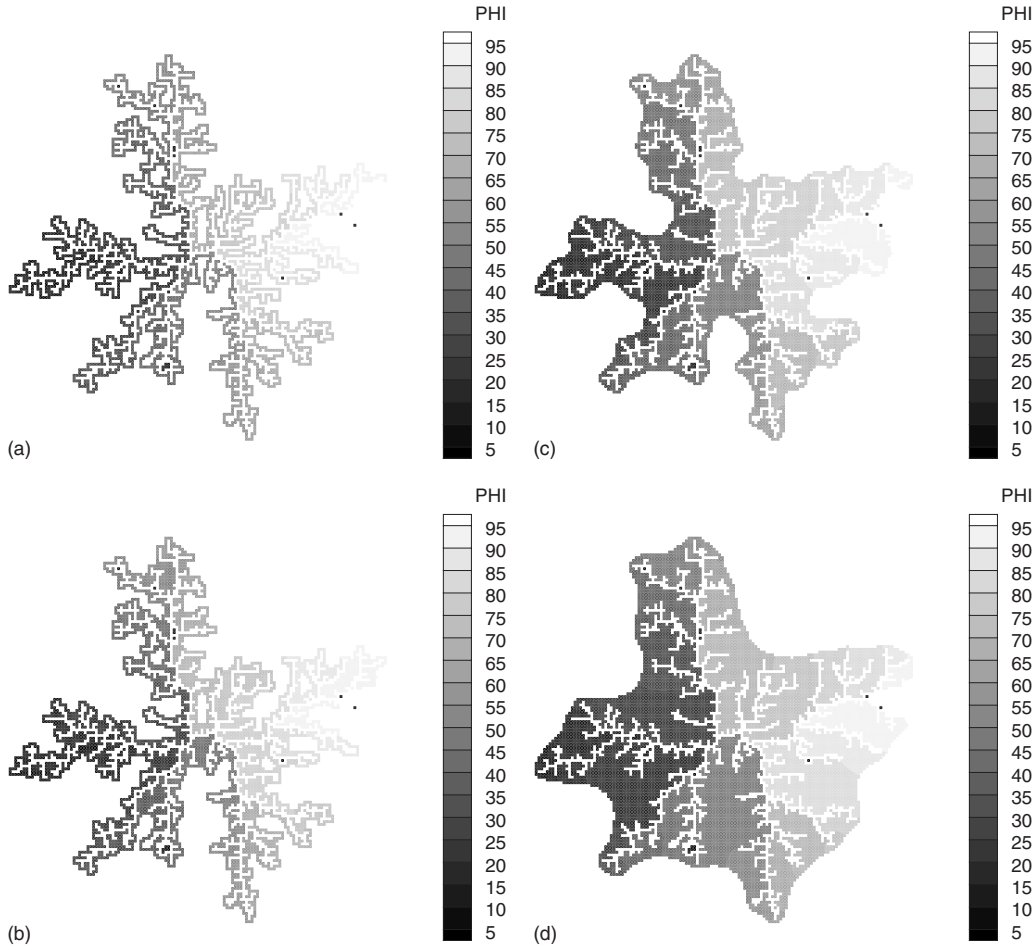


FIG. 4. Morphology of the adsorbed fluid on a 2D DLA of linear size $L=150$. As the filling fraction increases small scale features are smoothed out. The shading is the value of the velocity potential ψ . (a) $\phi=0.05$, (b) $\phi=0.10$, (c) $\phi=0.15$, (d) $\phi=0.20$.

ments in both 2D and 3D. The generators for the deterministic fractals [27] are shown in Fig. 2, along with the numerically calculated value of the exponent, ϵ_{num} , in the power law $\alpha \sim \phi^{-\epsilon}$. Also shown is the predicted value of the exponent from Eq. (1), ϵ_{pre} . This figure is placed here primarily for reference as in the text the fractals are referred to according to their position in the figure. Fractal 1 is associated with the top left generator in the figure. The generators are then counted by progressing along the rows, i.e., position (row 2, col 1) in the figure is fractal 4.

The black squares in the 2D generators are the solid material, and the generator is applied iteratively to the solid squares to give a fractal distribution of solid material. In the 3D case three cross sections of the generator are shown. The black squares again represent solid material and the generator is applied iteratively to these squares. An example for the 2D case is given in Fig. 3, which shows the generator and the resultant fractal at iteration number $n=4$. Stochastic fractals have also been considered and ten 2D and five 3D diffusion limited aggregation (DLA) clusters have been generated using the original algorithm of [28].

The lattice gas model only contains two free parameters, the fluid-solid interaction parameter, $y = w_{sf}/w_{ff}$, and the temperature T . Unless otherwise stated, the values of y and T are set at 2.0 and 0.8, respectively, with $w_{ff}=1$ being the energy

unit and w_{ff}/k_B the temperature unit. This temperature corresponds to $T/T_c=0.8$ in the 2D case and $T/T_c \approx 0.53$ in the 3D case, where T_c is the critical temperature for hysteresis.

A. Morphology of the adsorbed films

It was suggested in [29] that by increasing the filling fraction of adsorbed fluid in a fractal material, one could probe different length scales of the fractal geometry by defractalizing the object, but no evidence was provided that this was the case. Figure 4 shows the configuration of adsorbed fluid films at different filling fractions for a 2D DLA cluster of linear size $L=100$, whereby linear size is meant the diameter of a circle in which the DLA cluster fits. The particles in the DLA constitute the solid surface of the material.

As the filling fraction increases, the thickness of the film naturally increases smearing out the small scale features. Figure 4(c) shows the importance of the geometrical disorder. While there are large regions of the fractal where only a thin uniform film has developed on the fractal, there are “bottleneck” regions where fairly major condensation events have occurred and the “pore” has been completely filled with fluid. These avalanches of fluid are caused by the geometrical disorder of the system and the complex energy landscape this provides for the adsorbed fluid [20].

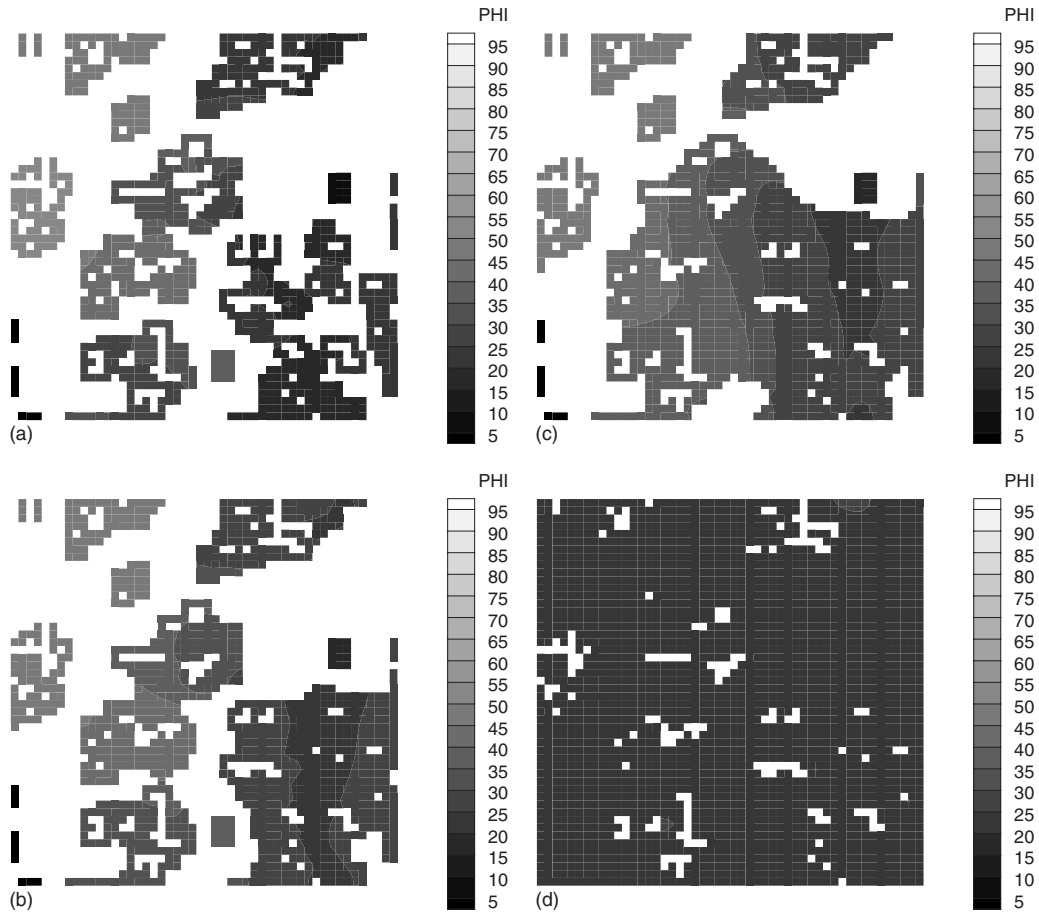


FIG. 5. Cross section taken at the center of the domain of an adsorption simulation for a 3D DLA cluster of linear size $L=50$ for $\gamma=2.0$ and $k_B T=0.8$. The shading in this case is the value of the velocity potential ψ . (a) $\phi=0.33$, (b) $\phi=0.47$, (c) $\phi=0.69$, (d) $\phi=0.94$.

Similar events occur in 3D, although these are harder to visualize. Figure 5 shows a 2D cross section, taken from an adsorption process in a 3D DLA cluster of linear dimension $L=50$. The first stage of the adsorption process is the formation of a liquid layer that coats the DLA cluster strands. As the filling fraction increases, the gaps between proximate groups of gel strands are bridged. The process is completed by a major final condensation event which fills the large void [23,30].

When compared to the adsorption patterns in deterministic fractals, it is clear that the disorder of the stochastic fractals has a large effect on the morphology of the adsorbed film. Figure 6 shows the adsorption pattern on a deterministic fractal, where the adsorption pattern is much more regular, in the sense that there is a strict symmetry imposed by the geometrical disorder.

These effects can also be observed in the adsorption isotherms of the systems. Figure 7 shows the adsorption isotherms for a 3D DLA cluster and deterministic fractal 7. The fluid morphology patterns described previously are clearly visible in the adsorption isotherms. The DLA clusters' isotherms show a slow adsorption at low chemical potentials (low filling fractions), which corresponds to the initial coating of the strands, and then gradually steepens as larger and larger crevices are filled in with fluid, until a final avalanche sweeps the whole system, as shown by the large final jump in

the adsorption isotherms. Note, however, that overall, the isotherm possesses a largely smooth characteristic, albeit a steepening one. On the other hand, the deterministic fractal isotherms have a much more stepped appearance, with the height of the steps gradually growing larger. This difference can be explained by the different range of length scales present in the different type of fractals. The deterministic fractal, due to its method of construction, contains features of a small number of length scales, whose number are equal to its iteration number. The steps in the adsorption isotherm can be viewed as points where there is a coherent filling of crevices of these length scales. This also explains the increasing size of the step height as larger and larger features of the deterministic fractal are filled. DLA clusters, on the other hand, have a much larger number of length scales and hence produce a smoother isotherm.

B. Fractal dimensions of the adsorbed fluid

1. Box counting dimension D_f

A more quantitative analysis of this defractalization can be performed by box counting [31] the fluid morphology at different filling fractions and observing the variation of the fractal dimension and the range of length scales, a to δ_{max} , over which fractal behavior can be observed. Figure 8 shows results from the box counting algorithm for different filling

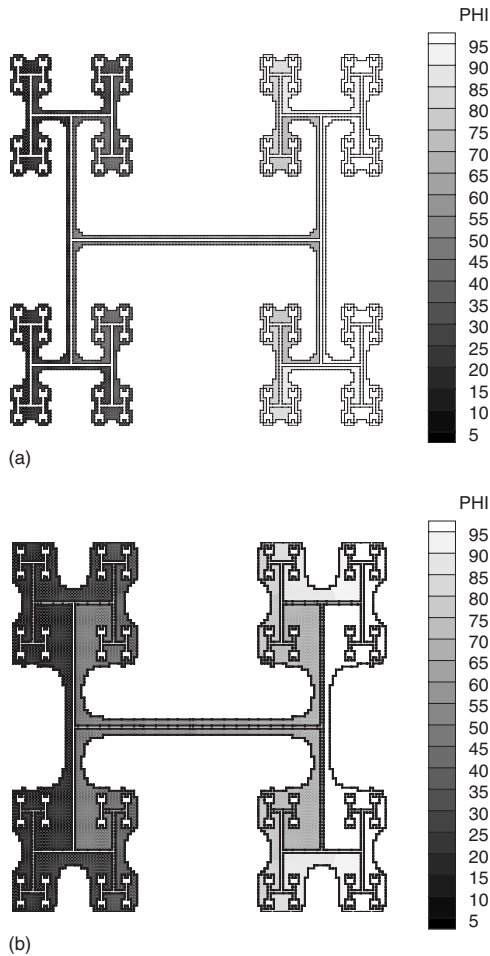


FIG. 6. Morphology of the adsorbed fluid on a deterministic fractal of linear size $L=126$. (a) $\phi=0.17$ (b) $\phi=0.32$.

fractions for a 3D DLA cluster and a 3D deterministic fractal (fractal number 7). At low filling fractions a clear power law with a noninteger exponent is visible for over a decade of length scales. As the filling fraction is increased the upper limit of fractal behavior δ_{max} remains unchanged, while the lower limit a progressively becomes greater. Eventually, a point is reached where it becomes meaningless to talk of a

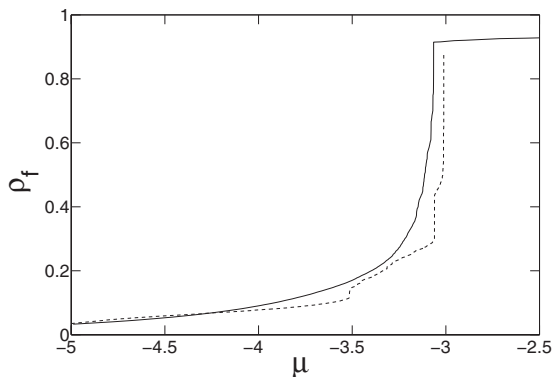


FIG. 7. Adsorption isotherms for 3D deterministic (dashed line) and DLA (solid line) fractals. Deterministic fractals display a more stepped adsorption isotherm than stochastic fractals.

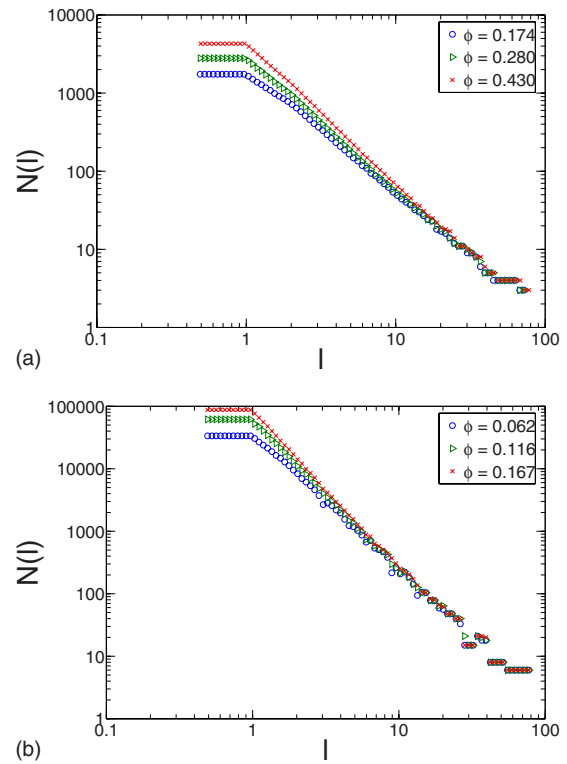


FIG. 8. (Color online) Results from the box counting algorithm showing the number of boxes $N(l)$ of size l required to cover the fluid for (a) a 2D DLA cluster of linear size $L=100$ and (b) a 3D deterministic fractal (fractal number 7) of linear size $L=81$. In both cases it is clear how the minimum length scale at which fractal behavior is observed increases with filling fraction.

fractal regime, as the extent over which the noninteger exponent can be observed becomes too small. The box counting results with $\phi=0.430$ show an example of such a regime, where the adsorbed fluid is Euclidean with dimension 2.

Figure 9 shows the minimum length scale a for which power law behavior is observed as a function of ϕ for a 2D DLA cluster and deterministic fractal 1. In the case of the

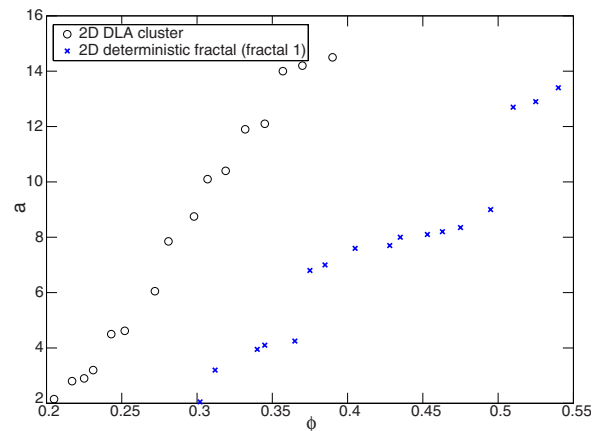


FIG. 9. (Color online) The minimum length scale a at which fractal behavior can be observed against the filling fraction for (a) a 2D DLA cluster of linear size $L=100$ and (b) a 2D deterministic fractal (fractal number 1) of linear size $L=125$.

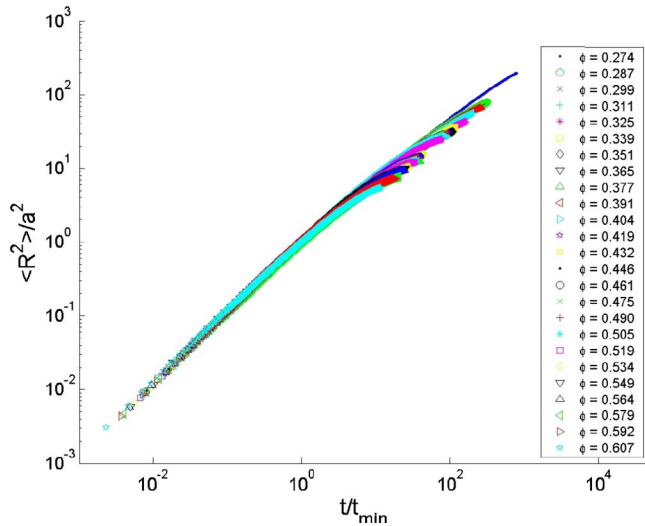


FIG. 10. (Color online) Results from the exact enumeration on a 2D DLA cluster of linear size $L=100$ for a range of filling fractions $\phi=0.274$ to 0.432.

DLA cluster the increase of a is fairly smooth with filling fraction, whereas in the case of the deterministic fractal, three clear jumps in a can be observed with a remaining relatively constant in between these jumps. The magnitude of these jumps increases with increasing filling fraction. This behavior is not surprising given the different nature of the stochastic and deterministic fractals and is another manifestation of the effect of the limited number of discrete scales of the deterministic fractal (in this case three scales). The stepped nature of the minimum length scale is the same effect as the stepped nature of the adsorption isotherm for the deterministic case, in that the discrete scales of the deterministic fractals seem to be removed by an avalanche of fluid which causes a sudden jump in a . On the other hand the smooth adsorption isotherm of the stochastic fractals is reflected in the smooth nature of the increase of a .

2. Random walk dimension D_w

In order to compare the predicted exponent of the scaling of tortuosity with filling fraction from Eq. (1), it is necessary to perform random walks on the adsorbed fluid morphologies. This is achieved using the exact enumeration algorithm described in [32]. In both 2D and 3D cases, random walks of length $N=5000$ are performed. Typical results are shown in Fig. 10 for the scaled variables $\langle R^2 \rangle / a^2$, where $\langle R^2 \rangle$ is the mean square distance of the random walker, and t/t_{min} , where t_{min} is the average time taken at a given filling fraction for the random walker to diffuse a distance a . Qualitatively identical results are obtained for all fractals in both 2D and 3D. The use of the scaled variables collapses all the data from all filling fractions onto a single curve, with the expected departures at large times, where the random walker begins to reach the edge of the finite size adsorbed fluid. The value of D_w is extracted by finding the slope of the ensemble average squared distance with the scaled time for all filling fractions up to which fractal behavior can be observed, in the regime $1 < \langle R^2 \rangle / a^2 < \delta_{max}^2 / a^2$.

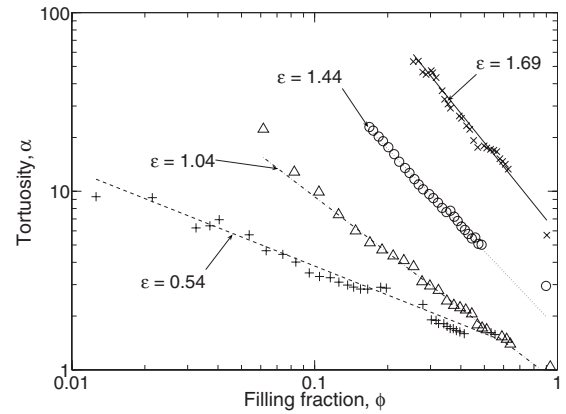


FIG. 11. Variation of tortuosity with filling fraction plotted on the log-log axes for (\times , solid line) 2D deterministic (fractal 1) with $n=4$, (\circ , dotted line) 2D DLA cluster of linear size $L=100$, ($+$, dashed line) 3D deterministic (fractal 7) with $n=4$, and (Δ , dash-dot line) 3D DLA cluster of linear size $L=50$.

C. Numerically obtained variation of the tortuosity with filling fraction for adsorption

Initially, we shall only consider the variation of tortuosity with filling fraction in the case of adsorption. The desorption process is discussed below in detail. Figure 11 shows the variation for both 2D and 3D deterministic fractals (fractals 1 and 7, respectively) and DLA fractals and it is clear that all of the data is fitted by a power law of the form $\alpha \sim \phi^{-\epsilon}$. As expected the value of the exponents ϵ are significantly lower in the 3D cases when compared to the 2D cases. This is simply a manifestation of the fact that it is significantly easier to generate an obstacle to a 2D flow than to a 3D flow. The exponent for the 3D DLA cluster, $\epsilon=1.06$, is very close to the experimentally measured exponent of $\epsilon=1.16$ reported for aerogel in [10]. One surprising observation is again that the power law seems to extend in most cases (with the possible exception of the 2D DLA cluster) to filling fractions $\phi=\phi_c$. This is surprising, as one would expect any fractal characteristics of the fluid flow to be lost at much lower filling fractions, when the fractal nature of the adsorbed fluid is lost. However, the lack of data points means it is impossible to draw further conclusions about the behavior of the tortuosity at filling fractions where the adsorbed fluid no longer displays fractal behaviour.

D. Desorption and the effect of the fluid interaction parameter and the temperature

For the tortuosity to be a robust measure of the geometry of the porous material, it is crucial that its behavior is not affected by the nature of the adsorption or desorption process. The two free parameters of the LMFT theory model of sorption are the fluid interaction parameter, y , and the temperature, T . Simulations were performed at a range of y values and at different temperatures on both stochastic and deterministic fractals in 2D for both adsorption and desorption. Figure 12 shows the isotherms for a 2D DLA fractal of linear size $L=100$ for $y=1.5, 3$ and 5. Changing the value of the fluid-solid interaction has the effect of altering the nature of

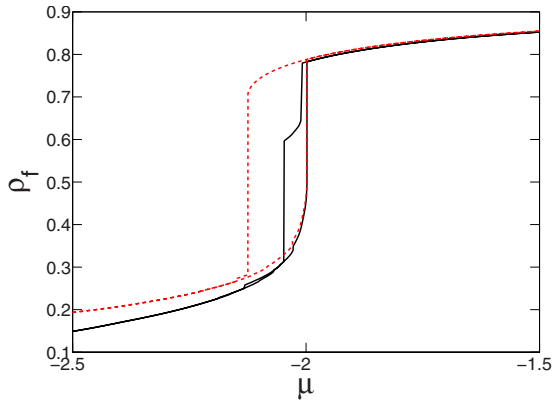


FIG. 12. (Color online) The sorption isotherms for a 2D DLA cluster of linear size $L=100$ for $y=1.5$ (solid line), and $y=3$ (dashed line). $T=0.8$ in both cases.

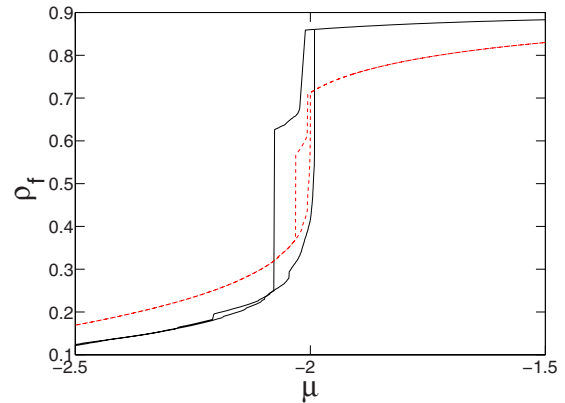


FIG. 14. (Color online) The sorption isotherms for a 2D DLA cluster of linear size $L=100$ for $T=0.6$ (dashed line) and $T=0.9$ (solid line). $y=1.5$ in both cases.

the sorption isotherm. The greatest hysteresis is observed at $y=3$, but there is significant hysteresis at the other values of y . The calculated tortuosities for both adsorption and desorption morphologies are shown in Fig. 13. It is clear that all of the adsorption morphologies follow a power law $\alpha \sim \phi^{-1.43}$ for all values of y , for all filling fractions up to $\phi=0.5$. However, there is a clear departure in the power law behavior for the desorption morphologies at filling fractions $\phi > 0.6$, although at lower filling fractions, the desorption morphologies also follow the power law $\alpha \sim \phi^{-1.43}$.

Similar patterns for the sorption isotherms for temperatures $T/T_c=0.4, 0.6, 0.7, 0.8$, and 0.9 for the same 2D DLA cluster can be seen in Fig. 14. As expected, the hysteresis decreases with increasing temperature, to the point where it has almost disappeared at $T/T_c=0.9$ (recall $T_c=1$ in the simple square 2D lattice). These isotherms show a similar trend of decreasing hysteresis with increasing temperature to those shown in [20] and this acts as a validation of the implementation of the LMFT model. Figure 15 shows the tortuosities obtained from these sorption isotherms for both adsorption and desorption. As in the case of varying y , all the

tortuosities follow a power law $\alpha \sim \phi^{-1.43}$ for $\phi < 0.6$, whereas for filling fractions larger than this only the adsorption morphologies follow this power law and the desorption morphologies show a markedly different behavior.

The filling fractions at which the desorption morphologies have tortuosities that differ from the power law $\alpha \sim \phi^{-1.43}$ can be seen to be those that correspond to fluid densities that are in the hysteresis regime, whether this hysteresis is caused by decreased temperature or increased fluid-solid interaction strength. If one examines these morphologies, the reason for the departure from the power law behavior is clear. Figure 16 shows the morphologies at nearly identical filling fractions for the adsorption and desorption isotherms, with (a) and (c) showing the adsorption branch and (b) and (d) the desorption branch at $y=1.5$ and $T=0.8$. Figures 16(c) and 16(d) show how the different mechanisms in the desorption process [30] affect the adsorbed fluid shape at virtually identical filling fractions. In the desorption case there is clearly a depinning transition associated with the gas reservoir interface as opposed to the more uniform film in the adsorption case. These

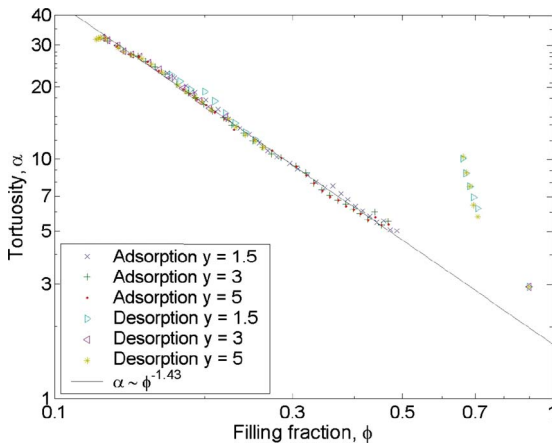


FIG. 13. (Color online) The variation of tortuosity corresponding for both adsorption and desorption, for $y=1.5, 3$, and 5 and $T=0.8$ in all cases. Tortuosities for the adsorption branches all follow $\alpha \sim \phi^{-1.43}$, while those from the desorption branches follow this law only for $\phi < 0.6$.

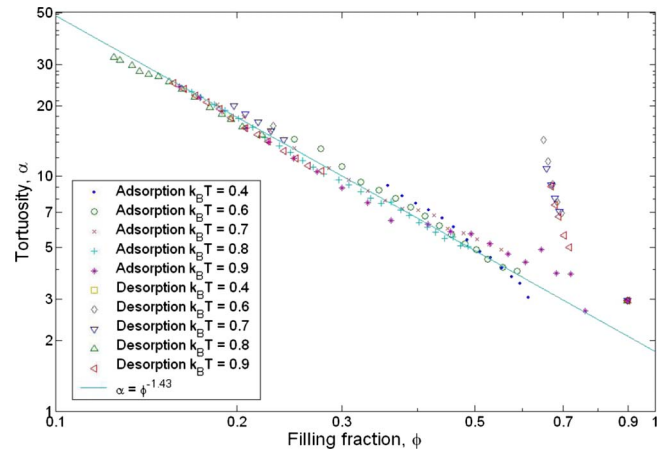


FIG. 15. (Color online) The variation of tortuosity corresponding to the sorption isotherms, i.e., both adsorption and desorption, for $T=0.4, 0.6, 0.7, 0.8$, and 0.9 and $y=1.5$ in all cases. Tortuosities for the adsorption branches all follow $\alpha \sim \phi^{-1.43}$, while those from the desorption branches follow this law only for $\phi < 0.6$.

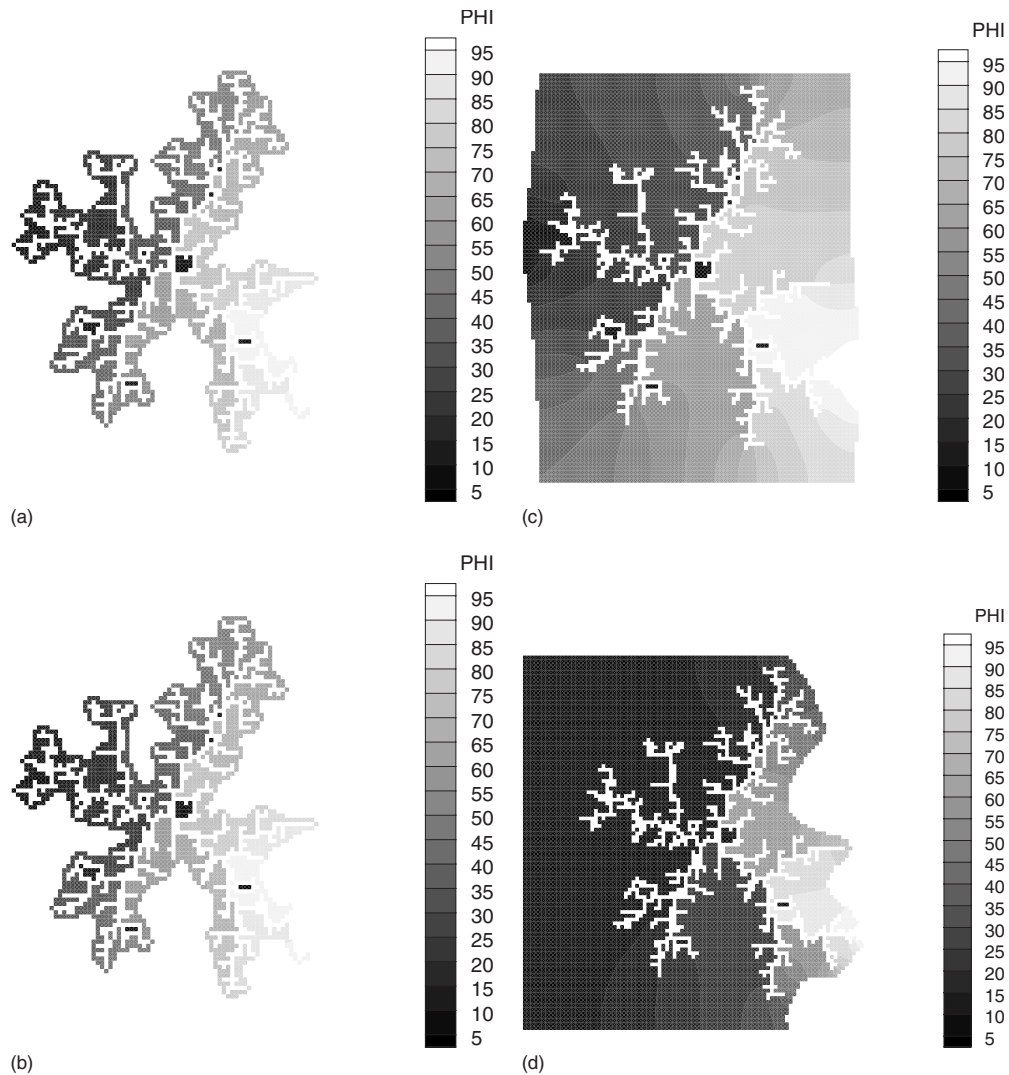


FIG. 16. Morphologies of the adsorbed fluid film for the sample 2D DLA cluster where (a) adsorption branch $\phi=0.189$ and (c) adsorption branch $\phi=0.684$. (b) desorption branch $\phi=0.187$ and (d) the desorption branch $\phi=0.689$ for $y=1.5$ and $T=0.8$. Shading is the velocity potential ψ .

different morphologies naturally give rise to different tortuosities. However, at the lower filling fractions shown in Figs. 16(a) and 16(b), when the hysteresis in the sorption isotherms is no longer present, the adsorbed fluid shape is largely the same regardless of whether it has been obtained from adsorption or desorption, and so at lower filling fractions the adsorption and desorption tortuosities agree.

E. Numerical and predicted scaling

Having the values of D_f and D_w for the adsorbed fluid allows the comparison of the numerical scaling with the scaling exponent predicted by Eq. (1). These results are shown in Fig. 17. The agreement between the predicted exponents and numerical exponents is generally good, especially for the DLA clusters, where the prediction is even sensitive to small changes in the numerical exponent of different DLA clusters. The maximum percentage difference between the predicted and numerical exponents for the DLA clusters is 7.6%. This is a promising result, as it suggests that the method is ca-

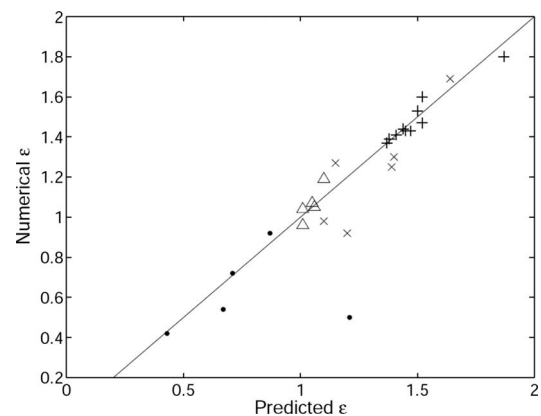


FIG. 17. Comparison of the numerically observed and predicted exponents for the unsaturated model. (\times) 2D deterministic fractals, ($+$) 2D DLA clusters, (\bullet) 3D deterministic fractals, and (Δ) 3D DLA clusters. The straight line predicted $\epsilon = \text{numerical } \epsilon$ again guides the eye.

pable of determining the different microstructure of different realizations of the same family of stochastic fractals. The agreement of the numerical and predicted exponents for the deterministic fractals is less impressive, although still in general good, with the exception of one fractal (fractal 10).

Excluding this point, the agreement between the predicted and numerical exponents is good over a wide range of the value of the exponent. Due to the limited number of deterministic fractals considered, it is difficult to say whether the predictions are more accurate for the 2D or 3D cases but it appears that the agreement in 3D is better. This observation, in tandem with the better agreement for the stochastic fractals, suggests that the predicted exponent is more accurate for highly porous materials. This could be linked to the presence of “loops” in the structure, that is regions where the fluid can be trapped for long periods of time, having a large impact on the observed tortuosity. Loops are unimportant in DLA clusters, as they are branching structures, and are also far more improbable in 3D structures when compared to 2D structures. D_w and D_f are certainly not sufficient to capture the presence of loops in a structure and the presence of loops could alter the scaling predicted in Eq. (1).

In general, the predicted exponent is an overestimate, and in the few cases where the numerical exponent is greater than the predicted one, it is by a relatively small amount when compared to the magnitude of the overestimation of the predicted exponent in some cases, i.e., there are more points further underneath the line predicted $\epsilon = \text{numerical } \epsilon$ in Fig. 17. Currently, we have no explanation for this.

V. CONCLUSIONS

It has been shown that a lattice gas model of adsorption combined with a simple finite element method describes ac-

curately the variation of tortuosity with liquid filling fraction in fractal materials. This defractalization process is a way of characterizing fractal materials over all length scales as smaller length scales are removed as the filling fraction increases. It was shown that the pertinent geometric disorder can be captured using a local mean field theory model. The scaling of tortuosity of the 3D DLA cluster with filling fraction obtained is in very close agreement with that obtained for aerogel in [10]. The value of the exponent changes for different realizations of the DLA cluster and also for different fractals and was shown to be independent of the model parameters γ and T . The exponent is the same for desorption and adsorption when the sorption isotherms coincide, i.e., in regions where no hysteresis is observed. The numerically calculated exponent also showed good agreement with the predicted values using Eq. (1), especially for the DLA clusters. The exponent ϵ is an important characteristic as it measures the impact of different length scales on the tortuosity of the material and is a measure of the multiscale nature of materials, which can be accessed experimentally. Further work is needed to understand why the predicted exponent is always an overestimate and what other fractal characteristics may be needed to more accurately predict ϵ .

ACKNOWLEDGMENTS

The authors are grateful to A. I. Golov, S. Babuin, and C. Ashton for many fruitful discussions. Both authors would like to acknowledge support under EPSRC Grant No. GR/S27559/01.

-
- [1] E. Anglaret, A. Hasmy, E. Courtens, J. Pelous, and R. Vacher, *J. Non-Cryst. Solids* **186**, 131 (1995).
 - [2] J. Banhart, *Prog. Mater. Sci.* **46**, 559 (2001).
 - [3] M. Sahimi, *Rev. Mod. Phys.* **65**, 1393 (1993).
 - [4] A.-L. Barabasi and H. Stanley, *Fractal Concepts in Surface Growth* (Cambridge University, Cambridge, England 1995).
 - [5] X. Zhang, M. Knackstedt, and M. Sahimi, *Physica A* **233**, 835 (1996).
 - [6] L. W. Hrubesh, *J. Non-Cryst. Solids* **225**, 335 (1998).
 - [7] P. Spanne, J. F. Thovert, C. J. Jacquin, W. B. Lindquist, K. W. Jones, and P. M. Adler, *Phys. Rev. Lett.* **73**, 2001 (1994).
 - [8] R. I. Al-Raoush and C. S. Willson, *J. Hydrol.* **300**, 44 (2004).
 - [9] A. E. Scheidegger, *The Physics of Flow through Porous Media* (University of Toronto Press, Toronto, 1974).
 - [10] S. Babuin and A. I. Golov, *J. Low Temp. Phys.* **134**, 333 (2004).
 - [11] D. Johnson, J. Koplik, and R. Dashen, *J. Fluid Mech.* **176**, 379 (1987).
 - [12] L. Landau and E. Lifshitz, *Fluid Mechanics* (Pergamon Press, New York, 1959).
 - [13] S. W. Coleman and J. C. Vassilicos, *Phys. Rev. Lett.* **100**, 035504 (2008).
 - [14] J. Feder, *Fractals* (Plenum Press, New York, 1988).
 - [15] S. Alexander and R. Orbach, *J. Phys. (France) Lett.* **43**, 625 (1982).
 - [16] R. Brown, *Geophysics* **45**, 1269 (1980).
 - [17] L. Rayleigh, *Philos. Mag.* **34**, 481 (1892).
 - [18] R. Dolesi, M. Bonaldi, and S. Vitale, *J. Low Temp. Phys.* **118**, 219 (2000).
 - [19] L. Gelb and K. Gubbins, *Langmuir* **15**, 305 (1999).
 - [20] F. Detcheverry, E. Kierlik, M. Rosinberg, and G. Tarjus, *Langmuir* **20**, 8006 (2004).
 - [21] L. Sarkisov and P. A. Monson, *Phys. Rev. E* **65**, 011202 (2001).
 - [22] E. Kierlik, M. Rosinberg, and G. Tarjus, *Europhys. Lett.* **62**, 337 (2003).
 - [23] R. Salazar and L. Gelb, *Mol. Phys.* **102**, 1015 (2004).
 - [24] E. Kierlik, M. Rosinberg, G. Tarjus, and E. Pitard, *Mol. Phys.* **95**, 341 (1998).
 - [25] O. C. Zienkiewicz and K. Morgan, *Finite Elements and Approximation* (Wiley Interscience, New York, 1983).
 - [26] D. L. Johnson and P. N. Sen, *Phys. Rev. B* **24**, 2486 (1981).
 - [27] T. Vicsek, *Fractal Growth Phenomena* 2nd ed. (World Scientific, Singapore, 1991).

- [28] T. A. Witten and L. M. Sander, *Phys. Rev. Lett.* **47**, 1400 (1981).
- [29] A. Golov, I. Berkutov, S. Babuin, and D. Cousins, *Physica B* **329-333**, 258 (2003).
- [30] F. Detcheverry, E. Kierlik, M. L. Rosinberg, and G. Tarjus, *Phys. Rev. E* **68**, 061504 (2003).
- [31] J. C. Vassilicos and J. G. Brasseur, *Phys. Rev. E* **54**, 467 (1996).
- [32] I. Majid, D. Ben-Avraham, S. Havlin, and H. E. Stanley, *Phys. Rev. B* **30**, 1626 (1984).